# Thermosolutal convection in a rectangular enclosure with strong side-walls and bottom heating

**M. S. Phanikumar**
CSIR Centre for Mathematical Modelling and Computer Simulation, National Aerospace Laboratories, Bangalore, India

Numerical solutions are presented for the problem of thermosolutal convection in a rectangular enclosure subjected to simultaneous heating of the bottom and sidewalls. A steady model based on primitive variables and an unsteady model solved using a high-accuracy numerical scheme are used to study the problem. Effects of the Lewis number, buoyancy ratio, aspect ratio and the Rayleigh number on flow and heat and mass transfer rates are studied. Details of oscillatory solutions and flow bifurcations are presented.

**Keywords:** convection; numerical methods; steady-state; thermosolutal; transient; instability; chaos; flow bifurcations

## 1. Introduction

Thermosolutal convection in enclosures is of fundamental importance in such diverse areas as crystal growth, solar ponds, casting of alloys and mining of gas caverns for oil storage. In nature, thermosolutal convection occurs in the oceans, shallow water bodies, magma chambers and the earth's crust (mantle convection).

Over the past several years, substantial progress has been made in understanding combined natural convection for cases in which gradients of temperature and species concentration are either vertical or horizontal (Chang et al. 1993, Béghein et al. 1992, Han and Kuehn 1990, Weaver and Viskanta 1991a, 1991b, Trevisan and Bejan 1987, Kamotani et al. 1985). While the effect of lateral heating on a double-diffusive system has been studied (Bergman and Ungan 1988), not much attention has been paid to the problem of thermosolutal convection in an enclosure for cases in which gradients of temperature or concentration cannot be strictly classified as being vertical or horizontal. The aim of this paper is to report on convection in an enclosure whose bottom and sidewalls are strongly heated, while the left wall is maintained at a higher level of concentration compared to the right one. This problem differs from the classical Rayleigh-Bénard situation in that motion immediately ensues for any nonzero Rayleigh number. The present problem is of considerable importance in understanding the effects of mass transfer on flow during contact metamorphism in geophysics (Furlong et al. 1992), in the design of heat recovery systems (Reay 1979) and furnace heat transfer, design and fenestration.

In practice, thermal boundary conditions considered in the present work are realized when an enclosure made of a high thermal conductivity material is heated from the bottom, resulting in a uniform sidewall and bottom temperature. In the field of geophysics, most cases of contact metamorphism are known to be characterized by strong lateral thermal gradients in addition to mass transfer between the host rock and the fluid. This work represents a first step toward constructing realistic thermal models of metamorphic terranes (e.g., models that take rock porosity and permeability into account).

In the field of crystal growth, it is widely acknowledged that solute segregation and defect density have a direct bearing on the quality of the crystal. To increase compositional uniformity and enhance crystal integrity, it is important to understand the role of convection in the melt (Ostrach 1983). Since the Czokralski crystal growth technique is characterized by heating of the ampoule walls and bottom, the present work should be of help in understanding the effects of a horizontal solute gradient on flow in the ampoule. Surface striations caused by oscillations due to thermal and species buoyancy are generally known to have a deleterious effect on growth of the crystal and, hence, conditions that give rise to oscillatory solutions are important from a practical point of view.

One aspect of the present problem that makes it particularly difficult lies in the fact that heating an enclosure both from the bottom and the sides makes the flow unsteady. Hence, steady-state solutions cannot be expected for all values of the Rayleigh number. Hence, a time-dependent model has been employed in the present work to capture the unsteady solutions. Since information on the nature of the oscillatory solutions (e.g., time series, phase plane behavior, etc.) is important both from theoretical and practical points of view, these issues are examined at length in a subsequent section.

Even though chaos in thermosolutal convection was first established ten years ago (Moore et al. 1983), details of the underlying mechanism are being understood only recently (Chang and Lin 1993). Much of the earlier work done in this area is concerned with buoyant flow of a single-component fluid and some of the important work done is summarized in the excellent review article by Yang (1988). The presence of an

Address reprint requests to Dr. Phanikumar at the CSIR Centre for Mathematical Modelling and Computer Simulation, National Aerospace Laboratories, Bangalore 560 037, India.

Received 18 May 1993; accepted 7 March 1994

additional source of buoyancy that can augment or oppose that due to temperature alone, and large differences in the diffusivities of heat and mass, can greatly complicate multicomponent convection. The phenomena of salt fountains, salt fingers and sharp diffusive interfaces offer some examples of the way in which nonlinearities of the system can get manifested. Carefully conducted laboratory experiments and numerical simulations provided ample evidence to the fact that thermosolutal convection is an inherently unstable phenomenon (Turner 1975, Jiang et al. 1988). A survey of the existing literature showed that studies aimed at understanding the complex phenomenon of instability in thermosolutal convection are relatively few in number. One of the aims of this paper is to report on oscillatory convection in an enclosure and to study the flow bifurcations and route(s) to chaos.

Studies of transitions and bifurcations have been associated with the onset of turbulence for a long time. However, solutions reported here exhibit only temporal nonperiodicity (chaos) with some broadband noise and hence, as Yang (1988) points out, such cases represent, at best, only weak turbulence, not full turbulence due to lack of the corresponding spatial behavior. For single-component convection, several routes to turbulence have been proposed earlier and many of them have been observed experimentally. The scenario proposed by Feigenbaum (1979) and Ruelle et al. (1978) are well known. In the Feigenbaum scenario, an infinite sequence of period doublings leads to turbulence. Hence, a stable steady-state ($S$) solution precedes a simple periodic solution ($P$, in the notation of Gollub and Benson 1980), which in turn precedes solutions corresponding to subharmonic bifurcations ($P_2, P_4, \ldots$). At the end of this sequence is the nonperiodic or chaotic regime, $N$. In the Ruelle-Takens-Newhouse (RTN) scenario, only three Hopf bifurcations are needed to reach $N$. This route is represented by $S \rightarrow P \rightarrow QP_2 \rightarrow N$, where $QP_2$ represents a quasi-periodic attractor.

It is now widely known that, even though Navier-Stokes equations have infinite degrees of freedom, turbulence in confined buoyant flows exhibits only a few of these (i.e., transition to turbulence would involve only a few bifurcations, but not infinitely as many as envisaged in the classical Landau-Hopf conjecture [Landau and Lifshitz 1982]). This has been confirmed by several carefully conducted experiments (e.g., Libchaber and Maurer 1982). This point has practical significance in that it opens up the possibility of modeling turbulence using essentially low-dimensional systems (e.g., a small number of ordinary differential equations) by projecting the Navier-Stokes equations on a low-dimensional space. To this end, understanding the confined buoyant-flow problem for various different initial and boundary conditions would be of great help. The present paper seeks to study the effects of heated confining sidewalls and a solute gradient on the classical Rayleigh-Bénard problem for the rigid-rigid case.

Earlier numerical and experimental studies for single-component convection showed that subharmonic bifurcations are very sensitive to details of spatial structure and are mainly caused by corner vortices (Kessler 1987). Recent work on thermosolutal convection shows that the processes are much more complex, involving the interaction of the thermal and solutal boundary layers. This interaction was found to generate secondary flows with periodically separating blobs. These seiche fluctuating modes are believed to be related to the swaying of the unsteady solutal boundary layer (Chang and Lin 1993).

In spite of the fact that several theories are being put forward to explain the observed phenomenon of thermosolutal convection, there is a need to carry out fundamental studies related to instability and transition. One of the reasons for this lies in the fact that numerical simulations do not always capture the real instabilities and routes due to false diffusion inherent in most numerical schemes. For instance, it is not uncommon to find that period doublings and chaos are a purely numerical artifact exhibited by finite-difference equations, while their continuum counterparts are not known to show any such behavior. (See Lorenz 1989 for one such example, the logistic equation.) It is from this point of view that a high-accuracy numerical scheme is employed in the present work to study the oscillatory solutions.

## 2. Steady two-dimensional convection

### 2.1. Mathematical model

Consider a rectangular enclosure (Figure 1) whose four sides are all isothermal. We assume that the enclosure is infinitely

**Notation**

| | |
|---|---|
| $AR$ | Aspect ratio, $H/L$ |
| $C$ | Dimensionless concentration |
| $D$ | Diffusion coefficient |
| $F$ | First derivative of stream function, Equation 30 |
| $g$ | Gravitational acceleration |
| $\mathrm{Gr}_T$ | Thermal Grashof number ($g\beta_T \Delta T L^3/\nu^2$) |
| $\mathrm{Gr}_S$ | Solutal Grashof number ($g\beta_C \Delta C L^3/\nu^2$) |
| $h$ | Heat transfer coefficient |
| $h_1$ | First space step near a wall, Equation 29 |
| $h_m$ | Mass transfer coefficient |
| $H$ | Height of enclosure |
| $K_1, K_2$ | Constants defined in Equation 13 |
| $L$ | Width of enclosure |
| Le | Lewis number ($\alpha/D$) |
| $N$ | Buoyancy ratio ($\mathrm{Gr}_S/\mathrm{Gr}_T$) |
| $\mathrm{Nu}_x$ | Local Nusselt number ($h(x)L/k$) |
| $\underline{\mathrm{Nu}}_y$ | Local Nusslet number ($h(y)H/k$) |
| $\overline{\mathrm{Nu}}$ | Mean Nusselt number |
| $P$ | Dimensionless pressure ($P'L^2\rho/\mu^2$) |
| Pr | Prandtl number ($\nu/\alpha$) |
| $\mathrm{Ra}_T$ | Thermal Rayleigh number ($\mathrm{Gr}_T\mathrm{Pr}$) |
| $S$ | Second derivative of stream function, Equations 31–33 |
| Sc | Schmidt number ($\nu/D$) |
| $\underline{\mathrm{Sh}}_y$ | Local Sherwood number ($h_m H/D$) |
| $\overline{\mathrm{Sh}}$ | Mean Sherwood number |
| $t$ | Time (s) |
| $T$ | Dimensionless temperature |
| $u, v$ | $X$ and $Y$ components of velocity |
| $Y_{max}$ | Extent of domain in $Y$ direction |

*Greek symbols*

| | |
|---|---|
| $\alpha$ | Thermal diffusivity |
| $\beta_T$ | Volumetric expansion coefficient, $(T) = -\frac{1}{\rho}\left(\frac{\partial \rho}{\partial T}\right)_{P,C}$ |
| $\beta_C$ | Volumetric expansion coefficient, $(C) = +\frac{1}{\rho}\left(\frac{\partial \rho}{\partial C}\right)_{P,T}$ |
| $\gamma$ | Tuning parameter defined in Equation 13 |
| $\rho$ | Density |
| $\tau$ | Dimensionless time ($t\nu/L^2$) |
| $\nu$ | Kinematic viscosity |
| $\xi, \eta$ | Dummy variables defined in Equation 13 |
| $\zeta$ | Dimensionless vorticity ($\zeta' L^2/\nu$) |
| $\psi$ | Dimensionless stream function ($\psi'/\nu$) |
| $\lambda$ | Wachspress iteration parameter, Equation 32 |

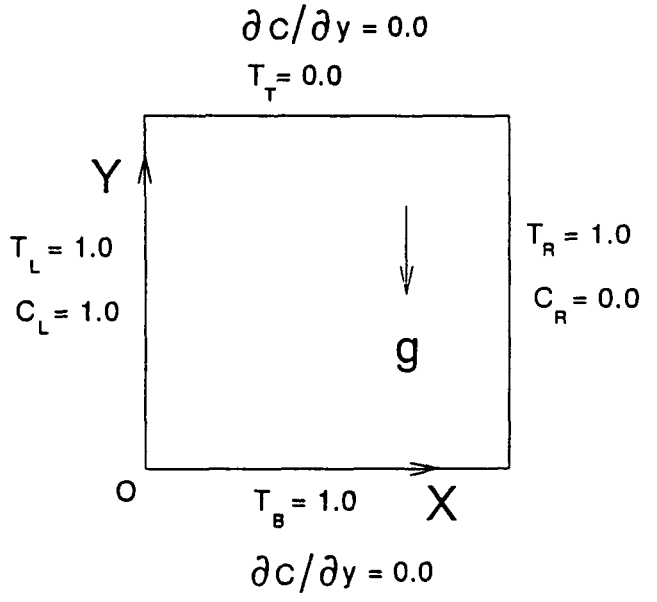


*Figure 1* Geometry and coordinate system

long in the $Z$-direction (perpendicular to the plane of the paper) so that the flow may be treated as being two-dimensional. The left, right and bottom walls of the enclosure are heated, while the top wall is at ambient temperature. The left sidewall is maintained at a higher level of concentration compared to the right one. The top and bottom walls are solute impermeable. We assume that the flow is laminar and incompressible and that the Dufour, Soret, viscous dissipation and variable property effects are all negligible. In addition, we assume that the enclosure walls are impermeable. While this assumption seems to be contradictory to that of the existence of mass transfer through the walls, Trevisan and Bejan (1987) have shown (using scale analysis) that it is valid when the Lewis number is sufficiently high or when the solution is dilute (or both). Since the present work is concerned with situations in which the Lewis number is much greater than unity (Le $\sim$ 100 is chosen to represent the water-salt system), we are justified in modeling the walls as being impermeable. With these assumptions, the steady governing equations, written using the primitive variables, appear as follows.

*Energy*:

$$u\frac{\partial T}{\partial X}+v\frac{\partial T}{\partial Y}=\mathrm{Pr}^{-1}(\nabla^2 T) \tag{1}$$

*Species concentration:*

$$u\frac{\partial C}{\partial X}+v\frac{\partial C}{\partial Y}=\mathrm{Sc}^{-1}(\nabla^2 C) \tag{2}$$

*Momentum:*

$$u\frac{\partial u}{\partial X}+v\frac{\partial u}{\partial Y}=-\frac{\partial P}{\partial X}+(\nabla^2 u) \tag{3}$$

$$u\frac{\partial v}{\partial X}+v\frac{\partial v}{\partial Y}=-\frac{\partial P}{\partial Y}+(\nabla^2 v)+(\mathrm{Gr}_T T-\mathrm{Gr}_S C) \tag{4}$$

Here,

$\mathrm{Gr}_T=g\beta_T\Delta T L^3/\nu^2$, $\mathrm{Gr}_S=g\beta_C\Delta C L^3/\nu^2$,

$T=(T'-T'_L)/\Delta T$, $C=(C'-C'_L)/\Delta C$,

$X=x/L, Y=y/L$, $u=u'/U$, $v=v'/U$ and $U=\nu/L$

Primes in these quantities denote dimensional variables. $\Delta T$ and $\Delta C$ are the maximum temperature and concentration differences in the system given by $\Delta T=(T_L-T_T)$ and $\Delta C=(C_L-C_R)$. Boundary conditions for the above system of equations are given in Equations 5–8.

$$X=0(\forall Y)\text{: } T=1,\ C=1 \tag{5}$$

$$X=1(\forall Y)\text{: } T=1,\ C=0 \tag{6}$$

$$Y=0(\forall X)\text{: } T=1,\ \frac{\partial C}{\partial Y}=0 \tag{7}$$

$$Y=1(\forall X)\text{: } T=0,\ \frac{\partial C}{\partial Y}=0 \tag{8}$$

For the boundary conditions in Equations 5–8, flows resulting from concentration and temperature differences can either augment or oppose each other depending on whether the buoyancy ratio $N(=\mathrm{Gr}_S/\mathrm{Gr}_T)$ is negative or positive. (Note the definitions of volumetric expansion coefficients associated with temperature and species given in the nomenclature.) We also note that the words *aiding* or *opposing* refer to the action of buoyancy at the left sidewall and that the solution for one case is the laterally inverted solution of the other. Hence, changing the sign of the buoyancy ratio has the effect of interchanging the left and right wall Nusselt numbers while the bottom Nu and the left wall Sherwood number do not change. This point has been actually verified by obtaining solutions over a wide range of buoyancy ratios. In view of this symmetry around $N=0$, we consider only the opposing flow regime in this paper.

The local Nusselt and Sherwood numbers are evaluated using the following equations.

$$\mathrm{Nu}_x=\begin{cases}-\left(\dfrac{\partial T}{\partial Y}\right)_{Y=0} & \text{bottom wall}\\ -\left(\dfrac{\partial T}{\partial Y}\right)_{Y=1} & \text{top wall}\end{cases} \tag{9}$$

$$\mathrm{Nu}_y=\begin{cases}-\left(\dfrac{\partial T}{\partial X}\right)_{X=0} & \text{left wall}\\ -\left(\dfrac{\partial T}{\partial X}\right)_{X=1} & \text{right wall}\end{cases} \tag{10}$$

$$\mathrm{Sh}_y=-\left(\frac{\partial C}{\partial X}\right)_{X=0}\quad\text{left wall} \tag{11}$$

Mean Nusselt and Sherwood numbers have been obtained by integrating along the wall. For instance, the following relation is used to obtain the average Nusselt number for the left wall.

$$\overline{\mathrm{Nu}_L}=\frac{1}{Y_{max}}\int_0^{Y_{max}}\mathrm{Nu}_y\,dY \tag{12}$$

## 2.2. Method of solution

Finite-difference forms of governing equations have been derived using microcontrol-volume integration. A staggered grid approach and the power law scheme have been used. The velocity-pressure coupling has been handled using the Semi-Implicit Method for Pressure Linked Equations—Revised (SIMPLER) algorithm (Patankar 1980). The resulting system of linear algebraic equations is solved iteratively by a line-by-line application of the tri-diagonal matrix algorithm. An additive correction (block correction) scheme has been used

to accelerate the rate of convergence (Settari and Aziz 1973). In view of the expected differences in the diffusivities of heat and mass, an efficient grid-clustering scheme is essential to resolve the length scales properly. We chose the Roberts transformation to do this (Roberts 1971). This transformation has several desirable properties, one of them being its ability to generate highly nonuniform grids such that steps increase linearly in the interior and much more rapidly near the walls (on a length scale on the order of the boundary-layer thickness, $\gamma$). For a given number of grid points, therefore, the tuning parameter $\gamma$ can be adjusted to achieve the desired resolution near the walls. Grids in $X$ and $Y$ directions have been generated using the uniformly spaced dummy variables $\xi(X)$ and $\eta(Y)$, respectively. For example, the following formula is used in the $Y$ direction.

$$Y_j = \frac{Y_{max}}{2} + K_1 \frac{e^{K_2} - 1}{e^{K_2} + 1}, \quad j = 2, 3, \ldots, NY \tag{13}$$

Here,

$$K_1 = \frac{Y_{max}}{2\sqrt{1 - 2\gamma/Y_{max}}}$$

and

$$K_2 = \left(\frac{2\eta_j}{Y_{max}} - 1\right) \ln\left(\frac{K_1 + Y_{max}/2}{K_1 - Y_{max}/2}\right)$$

$$\eta(Y) = \eta_j = (j - 1)\Delta\eta = \frac{Y_{max}}{(NY - 1)}$$

In Equation 13, $Y_j$ denotes the locations of the control volume faces, $NY$ denotes the number of points, $Y_{max} = H/L$, and $\gamma$ is a tuning parameter. As $\gamma \to 0$, the above formula generates very fine grids near the walls. Computations have been terminated when the relative error in the dependent variables is less than $10^{-6}$ between two successive iterations. It was also required that the maximum mass source should be less than $10^{-6}$ to declare convergence. Local Nusselt and Sherwood number data, spaced out at unequal intervals, have been integrated using an algorithm proposed by Gill and Miller (1972) to obtain the mean values.

### 2.3. Grid dependence studies and model validation

A series of numerical experiments have been carried out to make sure that solutions obtained are grid independent and accurate. An energy balance applied to the enclosure gives the conclusion that at steady-state, the algebraic sum of the Nusselt numbers evaluated on all the four walls should go to zero. That is to say,

$$\sum_{i=1}^{4} \overline{\mathrm{Nu}}_i = \varepsilon$$

where $\varepsilon$ should be a small number. In the present work, $\varepsilon$ as given here is found to be of the order of $10^{-5}$, thus indicating that the fluxes are conserved.

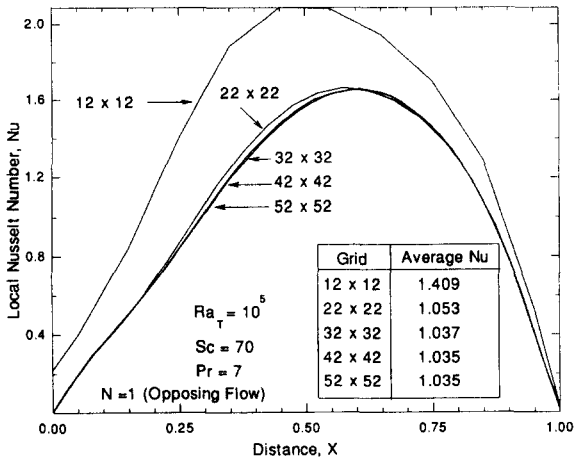


*Figure 2* Effect of grid size on the local Nusselt number distribution along the bottom wall for the case of combined convection (These results indicate that a 41 × 41 variable grid is adequate up to a Rayleigh number of $10^5$.)

Results obtained from the present algorithm have been compared with the benchmark solutions reported by de Vahl Davis (1983) for the case of pure natural convection in an enclosure. Excellent overall agreement between the solutions was obtained. The maximum difference in the mean Nusselt numbers was found to be less than 1 percent. Care has been taken to ensure that results obtained are independent of the grid parameters. Demonstration of grid independence for the present problem (combined convection) is provided in Figure 2, which shows variation of the local Nusselt number along the bottom wall. All computations reported in the present paper have been carried out using a 62 × 62 variable grid for an aspect ratio of 1.0. A 42($X$) × 162($Y$) variable grid is used for $AR = 4.0$. The tuning parameter $\gamma$ has been adjusted such that at least five control volumes are placed inside the thinnest of the boundary layers. A guideline for estimating the relative thicknesses of the thermal and concentration boundary layers has been obtained from the earlier work of Kamotani et al. (1985) who proposed the following relation:

$$\frac{\delta_T}{\delta_C} = [\mathrm{Le}\ N]^{0.25} \tag{14}$$

Further validation of the present model has been done by comparing the present solutions with the experimental work of Han and Kuehn (1991) for the case of combined convection in an enclosure with horizontal temperature and concentration gradients (Table 1). Excellent agreement has been obtained between the two results.

A few comments on the choice of the method of solution are in order. The major motivation for using the present (steady, iterative) approach lies in the ability to speed up the rate of convergence using an acceleration technique (here, block

**Table 1** Comparison of present numerical solutions with experimental data of Han and Kuehn (1991) for the case of combined convection in an enclosure with horizontal temperature and concentration gradients

| $AR$ | $\mathrm{Gr}_T$ | $\mathrm{Gr}_S$ | $N$ | Pr | Sc | $\overline{\mathrm{Nu}}$ Expt. | $\overline{\mathrm{Nu}}$ Present work | $\overline{\mathrm{Sh}}$ Expt. | $\overline{\mathrm{Sh}}$ Present work |
|---|---|---|---|---|---|---|---|---|---|
| 1.0 | $1.1 \times 10^6$ | $6.8 \times 10^6$ | −6.3 | 8.4 | 2420 | 9.5 | 9.30 | 83.0 | 83.83 |
| 1.0 | $3.7 \times 10^5$ | $3.2 \times 10^6$ | −8.6 | 8.5 | 2390 | 5.3 | 5.18 | 92.0 | 92.3 |
| 4.0 | $1.8 \times 10^5$ | $2.7 \times 10^6$ | −1.5 | 7.7 | 2400 | 20.8 | 20.63 | 121.0 | 121.98 |

correction). The time-marching approach based on the unsteady governing equations is found to be slow and time consuming. For a typical case (Le ~ 100, $Ra_T \sim 10^4$, $AR \sim 1$), the present algorithm is found to converge to a steady-state solution in about 800 iterations on a 62 × 62 grid. The unsteady approach, on the other hand, required about 50,000 iterations with a maximum allowable time step of $1 \times 10^{-5}$—a speed-up by a factor of about 50!

### 2.4. Results and discussion

**Pure thermal and pure species natural convection.** These two situations are important as they represent the limiting cases of $N = 0$ and $N = \infty$. For the pure heat transfer situation, shown in Figure 3(a), the fluid rises up along the heated sidewalls, hits the top wall and comes down in a jet along the centerline, thus forming two counterrotating cells. It is interesting to note that even though the thermal boundary conditions are symmetric around $X = 0.5$, the flow field at this Prandtl number is not symmetric. For the pure mass transfer case, the fluid sinks at the left wall, which is maintained at a higher level of concentration. For the range of $Gr_S$ considered in the present work, a single cell rotating in the counter-clockwise direction is obtained for Sc = 700. Heat transfer

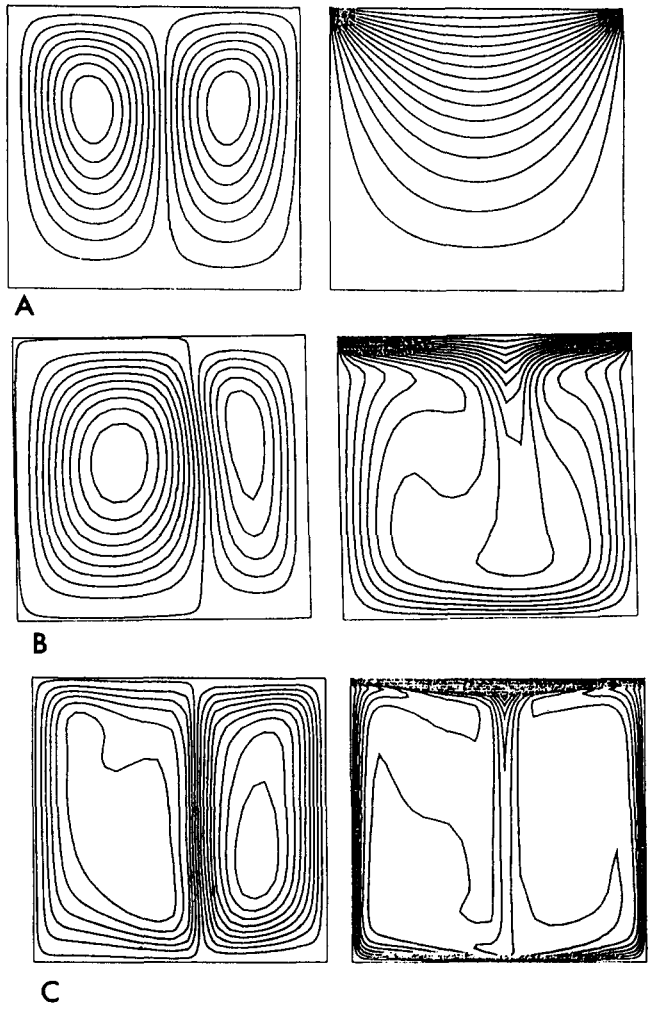


*Figure 3* Stream function and isotherm plots for the limiting case of pure thermal convection: (a) $Ra_T = 10^3$, (b) $Ra_T = 10^6$, (c) $Ra_T = 10^7$

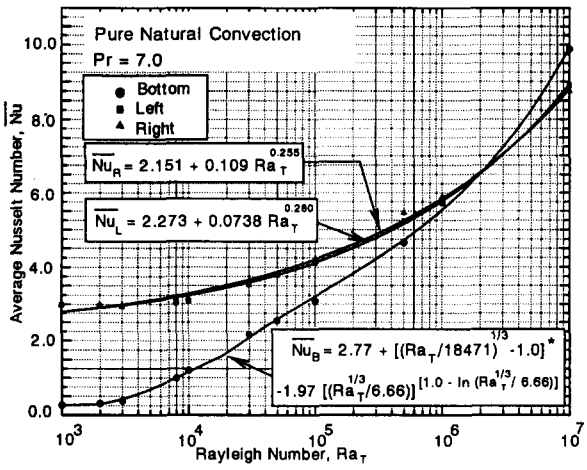


*Figure 4* Variation of average Nusselt numbers (for the left, right and bottom walls) as a function of the Rayleigh number for the case of pure thermal ($N = \infty$) convection (Pr = 7.0)

results for the case $N = 0$ can be accurately represented by the following correlations.

$$\overline{Nu}_L = 2.273 + 0.0738\ Ra_T^{0.280} \tag{15}$$

$$\overline{Nu}_R = 2.151 + 0.1090\ Ra_T^{0.255} \tag{16}$$

$$\overline{Nu}_B = 2.77 + \left[\left(\frac{Ra_T}{18471}\right)^{1/3} - 1\right]^* - 1.97\left(\frac{Ra_T^{1/3}}{6.66}\right)^{(1 - \ln(Ra_T^{1/3}/6.66)} \tag{17}$$

The notation [ ]* in Equation 17 implies that if tne quantity in the square brackets is negative, it should be taken as zero. These results are summarized in Figure 4. It can be seen that the bottom Nusselt number, which is initially much smaller compared to the left and right wall Nusselt numbers, increases gradually with the Rayleigh number and eventually becomes much higher than both these numbers. This is due to increased mixing caused by the descending plume of fluid, which jets down along the centerline and hits the bottom wall vigorously, thus causing an increase in the local Nusselt number around $X = 0.5$. (See Figures 3b and 3c.)

**Combined natural convection.** Each flow regime for the combined convection case can be uniquely identified by a set of five parameters: $Ra_T$, Pr, Le, $AR$ and $N$. Due to interest in water and fluids that closely represent water, the Prandtl number is fixed at 7.0. We now study, systematically, the effect of the remaining four dimensionless numbers on velocity, temperature and species concentration fields while keeping the other parameters fixed.

**Effect of the Lewis number.** Figure 5 shows effect of the Lewis number on flow, temperature and concentration fields for $Ra_T = 10^4$, $N = +1$ and $AR = 1$. For small Le, the flow is unicellular and in the counterclockwise direction, while at the highest Le considered in the present work (1,000), the flow exhibits two counter rotating cells. This is a consequence of the fact that thickness of the concentration boundary layer decreases with increasing Le, and in the limit as Le → ∞, the flow field becomes identical to the pure heat transfer case. The effect of the Lewis number on heat and mass transfer rates is summarized in Figure 6.

**Effect of the buoyancy ratio.** Figure 7 shows the effect of $N$ on flow, temperature and concentration fields for Le = 100 and $AR = 1$. The thermal Rayleigh number $Ra_T$ is

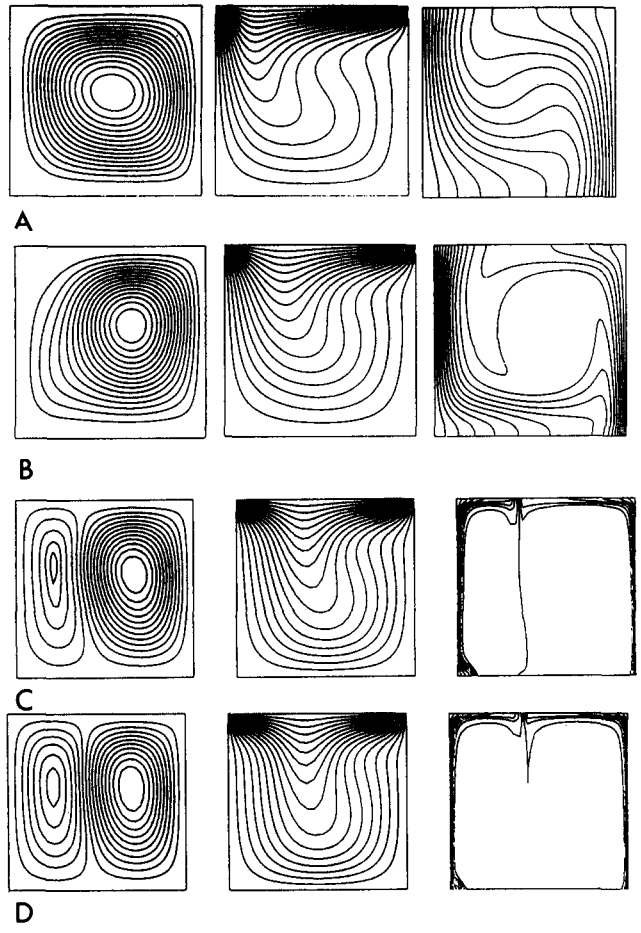


*Figure 5* Effect of the Lewis number on velocity, temperature and species concentration fields: (a) Le = 1, (b) Le = 100, (c) Le = 500, (d) Le = 1000 (This study has been carried out for $Ra_T = 10^4$, $N = 1$, $AR = 1$.)

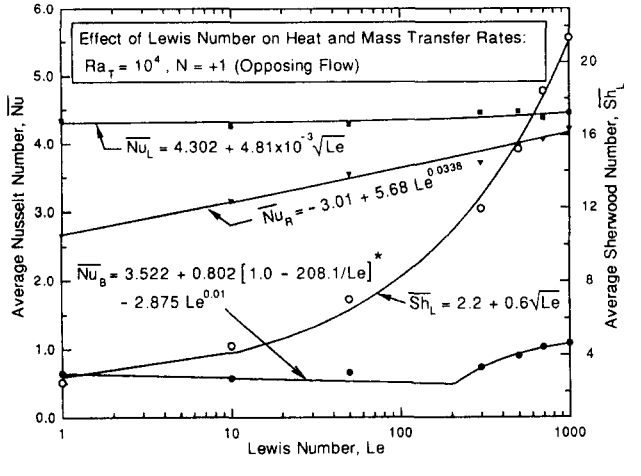


*Figure 6* Effect of the Lewis number on heat and mass transfer rates

fixed at $10^3$, while the solutal Rayleigh number is varied. The sequence of stream-function plots clearly shows a transition from the heat transfer-dominated situation ($N \sim 0$) characterized by the presence of two counter-rotating cells, to one dominated by mass transfer ($N \sim \infty$, single cell). We notice that the case $N = +30$ effectively represents the pure mass transfer case as can be seen from the distinct boundary layers on the sidewalls and the uniform core region. The effect of the buoyancy ratio on heat and mass transfer rates is summarized in Figure 8. Keeping the earlier observation regarding the symmetry of the flow around $N = 0$ in mind, we note that the heat and mass transfer data for the opposing case can also be used for the aiding case.

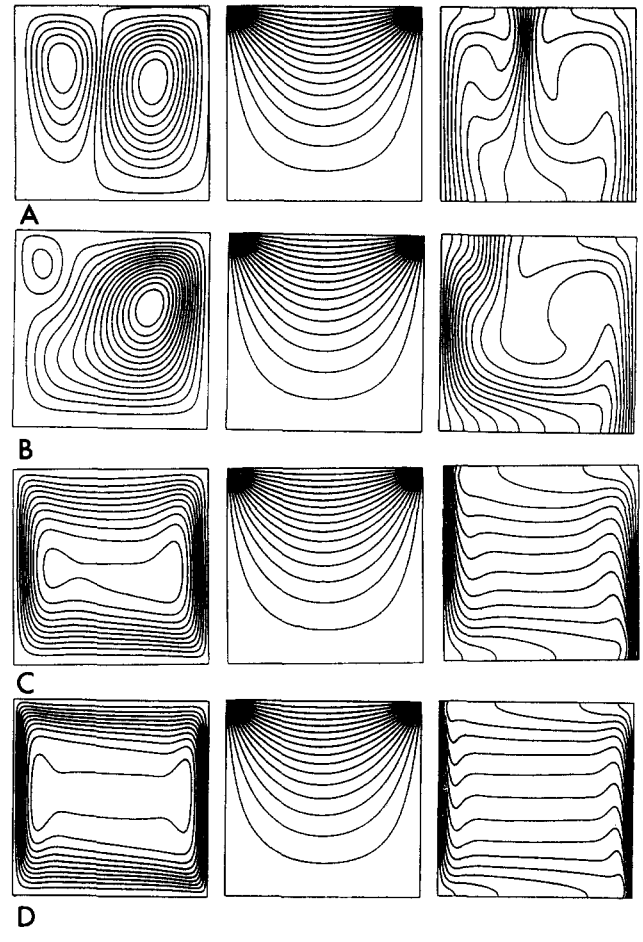


*Figure 7* Effect of buoyancy ratio ($N$) on velocity, temperature and species concentration fields: (a) $N = +0.1$, (b) $N = +0.5$, (c) $N = +5$, (d) $N = +30$ (The Rayleigh number $Ra_T$, Le and $AR$ are fixed at $10^3$, 100, and 1.0, respectively.)

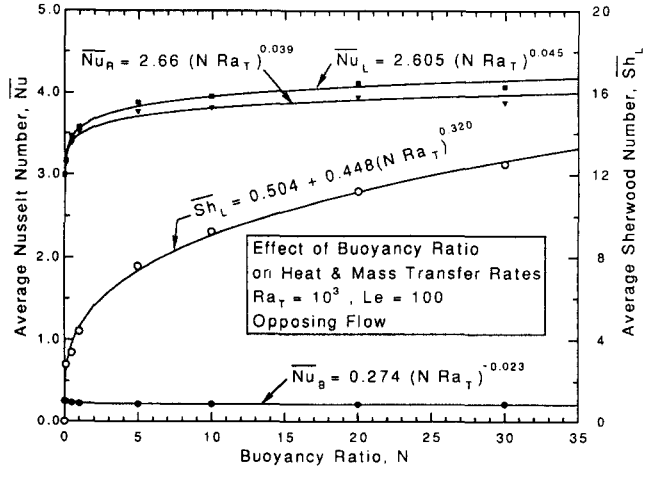


*Figure 8* Effect of the buoyancy ratio on heat and mass transfer rates

**Effect of the aspect ratio.** The effect of the aspect ratio is studied for $0.25 \leq AR \leq 4.0$. Figure 9 shows typical results for a shallow enclosure ($AR = 0.25$) and a deep one ($AR = 4$). For the shallow enclosure, we notice the presence of one recirculating cell on either side of the vertical wall and a low-velocity core region communicating with the cell at the right wall. The deeper enclosure, on the other hand, shows a relatively stronger circulation as can be seen from the steep gradients of species concentration near the sidewalls. Heat and mass transfer data, shown in Figure 10, suggest that there is a critical value of the enclosure aspect ratio beyond which the bottom behaves like an effectively insulated wall. This critical value of $AR$ is around 2.0. These results clearly indicate that the aspect ratio has a significant effect on heat and mass transfer rates.

**Effect of $Ra_T$.** Figures 11a–c show the effect of increasing $Ra_T$ for fixed values of $N(+1)$, Le (10) and $AR$ (1.0). As can be expected, strength of the recirculating cell increases with $Ra_T$,

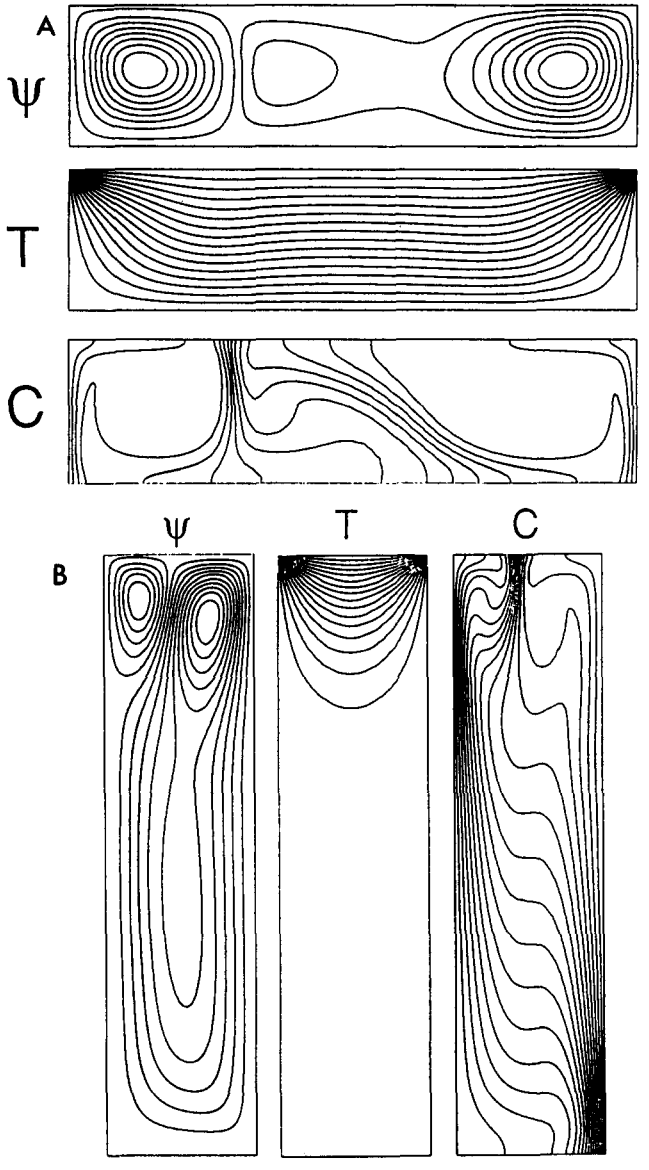


*Figure 9* Effect of the aspect ratio on velocity, temperature and concentration fields: (a) $AR = 1/4$, (b) $AR = 4$

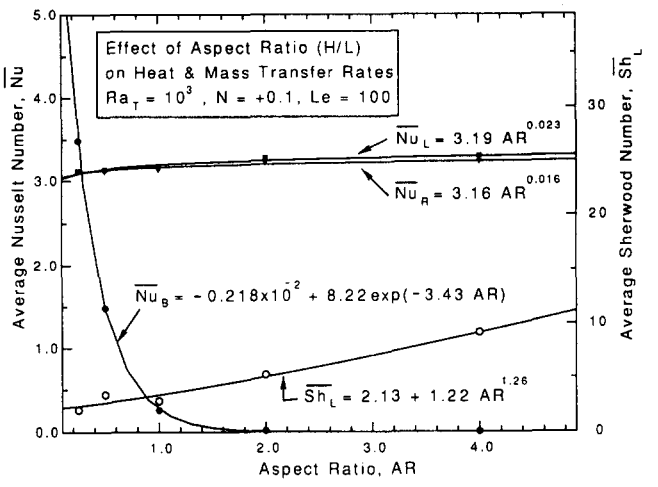


*Figure 10* Effect of the aspect ratio on heat and mass transfer rates

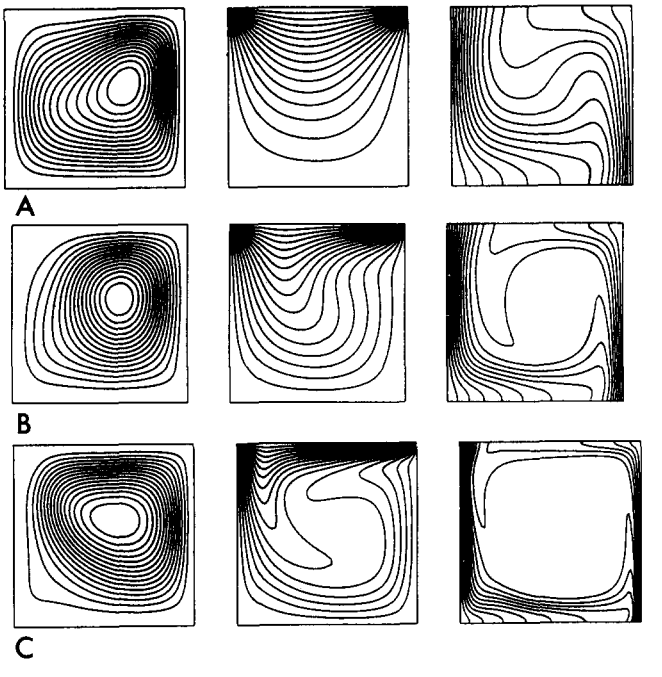


*Figure 11* Effect of $Ra_T$ on velocity, temperature and concentration fields: (a) $Ra_T = 10^3$, (b) $Ra_T = 10^4$, (c) $Ra_T = 10^5$ (Here Le, $N$ and $AR$ have been fixed at 10.0, 1.0 and 1.0, respectively.)

and since the solutal Rayleigh number also increases (to keep the ratio $N$ fixed), the concentration boundary layer becomes thinner. This behavior can be clearly seen from isopleths of concentration. Heat and mass transfer data are summarized in Figure 12. Stable steady-state solutions could not be obtained above $Ra_T = 10^6$. The mass residual (which gives an indication of convergence) and the velocity and species concentration are found to oscillate indefinitely.

Similarly, steady-state solutions could not be obtained in the Rayleigh number range $3 \times 10^3$–$3 \times 10^4$ for Le = 100 and $N = 1$. No attempt has been made to obtain the average Nusselt and Sherwood numbers in this range by integrating the time-dependent quantities over the period of oscillation.

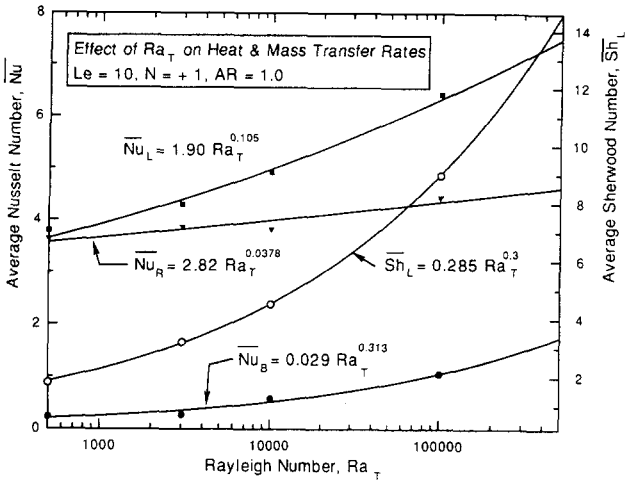


*Figure 12* Effect of $Ra_T$ on heat and mass transfer rates

## 3. Flow bifurcations and routes to chaos

### 3.1. Mathematical model

Consider the dissipative dynamic system represented by the following combined convection problem. The physical system considered here and the assumptions on which the model is based are essentially the same as in the previous section. The unsteady equations make use of the vorticity-stream-function approach.

*Energy:*

$$\frac{\partial T}{\partial \tau} + u\frac{\partial T}{\partial X} + v\frac{\partial T}{\partial Y} = \mathrm{Pr}^{-1}(\nabla^2 T) \tag{18}$$

*Species concentration:*

$$\frac{\partial C}{\partial \tau} + u\frac{\partial C}{\partial X} + v\frac{\partial C}{\partial Y} = \mathrm{Sc}^{-1}(\nabla^2 C) \tag{19}$$

*Vorticity transport:*

$$\frac{\partial \zeta}{\partial \tau} + u\frac{\partial \zeta}{\partial X} + v\frac{\partial \zeta}{\partial Y} = (\nabla^2 \zeta) - \mathrm{Gr}_T\left(\frac{\partial T}{\partial X}\right) + \mathrm{Gr}_S\left(\frac{\partial C}{\partial X}\right) \tag{20}$$

*Stream function:*

$$\nabla^2 \psi = \zeta \tag{21}$$

*Velocity:*

$$u = \frac{\partial \psi}{\partial Y} \tag{22}$$

$$v = -\frac{\partial \psi}{\partial X} \tag{23}$$

Here,

$\zeta = \zeta' L^2/\nu$, $\psi = \psi'/\nu$ and $\tau = t\nu/L^2$

All other quantities have been made dimensionless as in the previous section.

**Initial and boundary conditions.**

$$\tau = 0: u = v = T = C = \zeta = \psi = 0 \tag{24}$$

$$\tau > 0: X = 0(\forall Y): T = 1, C = 1, \psi = 0, \zeta = \zeta_w \tag{25}$$

$$X = 1(\forall Y): T = 1, C = 0, \psi = 0, \zeta = \zeta_w \tag{26}$$

$$Y = 0(\forall X): T = 1, \frac{\partial C}{\partial Y} = 0, \psi = 0, \zeta = \zeta_w \tag{27}$$

$$Y = 1(\forall X): T = 0, \frac{\partial C}{\partial Y} = 0, \psi = 0, \zeta = \zeta_w \tag{28}$$

The boundary vorticity $\zeta_w$ is evaluated using the following third-order accurate Padé approximant that was first proposed by Hirsch (1975, 1983).

$$\zeta_w = \frac{12}{h_1^2}[\psi_{w+1} + \psi_w] + \frac{6}{h_1}[(\psi_n)_{w+1} + (\psi_n)_w] + (\psi_{nn})_{w+1} + O(h_1^3) \tag{29}$$

In Equation 29, $h_1$ represents the space step near the wall and $n$ denotes the coordinate normal to the wall.

### 3.2. Method of solution

The numerical method used with this model is a combination of a second-order scheme (for solving the energy, concentration and vorticity equations) and a fourth-order compact Hermitian scheme for solving the stream-function equation. The higher order scheme assumes that in addition to the dependent variable, its first and second derivatives are also unknown in the domain of interest. One of the difficulties in implementing such a scheme lies in the specification of appropriate boundary conditions. Even though there exist higher order compact relations for calculating the boundary values of first and second derivatives, such methods are not always appealing from a physical point of view. The higher order method, when applied to the stream-function equation, does not suffer from such a drawback, because first and second derivatives of stream function are simply related to velocity and vorticity. The combined method compares favorably with a complete fourth-order scheme in terms of accuracy, while still retaining the basic advantage of a second-order method—its speed. For example, Bontoux et al. (1979) report that the combined method takes only 15 percent more computational time than a second-order scheme, while the fourth-order scheme takes about 280 percent more time. In the present work, the parabolic equations are solved by marching in time using the alternating direction implicit (ADI) scheme. The elliptic stream-function equation is solved iteratively using the ADI scheme with Wachspress parameters (Wachspress 1979). The following three-point relations connecting the function to its first and second derivatives form the basis of the higher order method (Hirsch 1983).

$$\frac{4}{(1+\beta_j)^2}F_{j+1} + 4F_j + \frac{4}{(1+\beta_j^{-1})^2}F_{j-1} + \frac{2}{(h_j + h_{j-1})} \times \left[-\frac{4}{(1+\beta_j)^2}(2+\beta_j^{-1})\psi_{j+1} + \frac{4(1-\beta_j^2)}{\beta_j}\psi_j + \frac{4}{(1+\beta_j^{-1})^2}(2+\beta_j)\psi_{j-1}\right] = 0 \tag{30}$$

$$\frac{1}{12}\left[\frac{\beta_j + 1 - \beta_j^{-1}}{1+\beta_j}S_{j+1} + (\beta_j + 3 + \beta_j^{-1})S_j + \frac{\beta_j^{-1} + 1 - \beta_j}{1+\beta_j^{-1}}S_{j-1}\right] - \frac{1}{(h_j h_{j-1})}\left[\frac{\psi_{j+1}}{(1+\beta_j)} - \psi_j + \frac{\psi_{j-1}}{(1+\beta_j^{-1})}\right] = 0 \tag{31}$$

$F$ and $S$ in Equations 30 and 31 represent the first and second derivatives, respectively, and $\beta_j = h_j/h_{j-1}$. After solving the

stream-function equation, the velocity field is calculated to fourth-order accuracy using the relation (Equation 30) for the first derivative and the definitions of the velocities (Equations 22 and 23). As an example of block compact integration of the stream-function equation, the following equations are obtained during the first half-step of the ADI scheme (implicit in the $X$ direction).

$$\lambda_k \psi^*_{i,j} - S^*_{x_{i,j}} = -\zeta^{n+1}_{i,j} + S^k_{y_{i,j}} + \lambda_l \psi^k_{i,j} \tag{32}$$

$$\frac{1}{12}\left[\frac{\beta_i + 1 - \beta_i^{-1}}{1+\beta_i} S^*_{x_{i+1,j}} + (\beta_i + 3 + \beta_i^{-1}) S^*_{x_{i,j}} + \frac{\beta_i^{-1} + 1 - \beta_i}{1+\beta_i^{-1}} S^*_{x_{i-1,j}}\right] - \frac{1}{(h_i h_{i-1})}\left[\frac{\psi^*_{i+1,j}}{(1+\beta_i)} - \psi^*_{i,j} + \frac{\psi^*_{i-1,j}}{(1+\beta_i^{-1})}\right] = 0 \tag{33}$$

In Equations 32 and 33, $S_x$ and $S_y$ denote the second derivatives of the stream function in the $X$ and $Y$ directions, respectively, and $\lambda$ represents the Wachspress iteration parameters. The superscripts * and $k$ denote the intermediate and previous time levels in the ADI step, while $n+1$ indicates that the most recently calculated values of vorticity are being used. The above 2 × 2 block tri-diagonal system is solved using von Rosenberg's bi-tridiagonal algorithm (von Rosenberg 1969). The Wachspress parameter significantly affects the overall speed of computations and for best results a sequence of these parameters should be used (Hageman and Young 1981).

### 3.3. Temporal and spatial grid refinement

The time step ($\Delta\tau$) used to integrate the unsteady equations has been chosen carefully. $\Delta\tau$ has been decreased until there is no appreciable change in the transient results. Step sizes used in the present work are typically on the order of $10^{-5}$. This value is decreased by a factor of ten during the initial period of simulations when the transient effects are expected to be strong.

Variable grids in both $X$ and $Y$ directions have been generated using Roberts' transformation (Equation 13). All computations carried out using the present combined scheme have been done using a 41 × 41 grid (except those for an $Ra_T$ of $10^6$, in which case a 61 × 61 grid was used), since the Rayleigh numbers considered here are quite low. It is well known that for a given accuracy, a second-order scheme requires about four times the number of grid points (in each direction) used with a fourth-order scheme. (See, for example, Hirsch 1983, p. 57.) Figure 2 clearly shows that a 41 × 41 variable grid is quite adequate for moderate values of $Ra_T$. Even though solutions reported in this section are of a mixed order (second plus fourth), these two facts taken together imply that the grid sizes used here are quite adequate.

The key to the success of the combined method lies in the higher order treatment of the boundary vorticity (Equation 29) and the higher order solution of the stream-function and velocity equations. This particular solution methodology, which combines an efficient grid-clustering scheme to place very fine grids near the walls together with the higher order method is believed to produce very accurate results.

### 3.4. Results and discussion

Since the Prandtl number is greater than 1.0, thermal effects are expected to play an important role compared to inertia effects. Furthermore, since the Schmidt number is greater than Pr, we expect that instability will be mainly caused by buoyancy due to species concentration. To reduce the numerical effort, we studied the problem for a square enclosure ($AR = 1$), Le = 100 and for $N = +1$. Furthermore, to understand the mechanism that leads to instability, we studied the time evolution of the various fields for a Rayleigh number ($Ra_T$) for which a steady-state solution could not be obtained earlier.

Figure 13 shows snapshots of the velocity, temperature and concentration fields for $Ra_T = 1.4 \times 10^4$ at different instants of time. We observe that the small-time behavior of the system is dominated by thermal convection (Figure 13a). As discussed in an earlier section, this flow is characterized by the presence of two counterrotating cells formed by fluid rising along the heated sidewalls. After this initial phase, two weak, solute-driven cells rotating in the counterclockwise direction are formed at the top and bottom corners of the left sidewall. Around $\tau = 2.5$, these cells merge together to form a single, strong cell at the left wall. This cell is basically driven by solutal buoyancy and rotates in the counterclockwise direction. The solution at this instant contains three cells, with the middle cell rotating in the clockwise direction and the other two cells rotating in a counterclockwise direction. After this phase, the

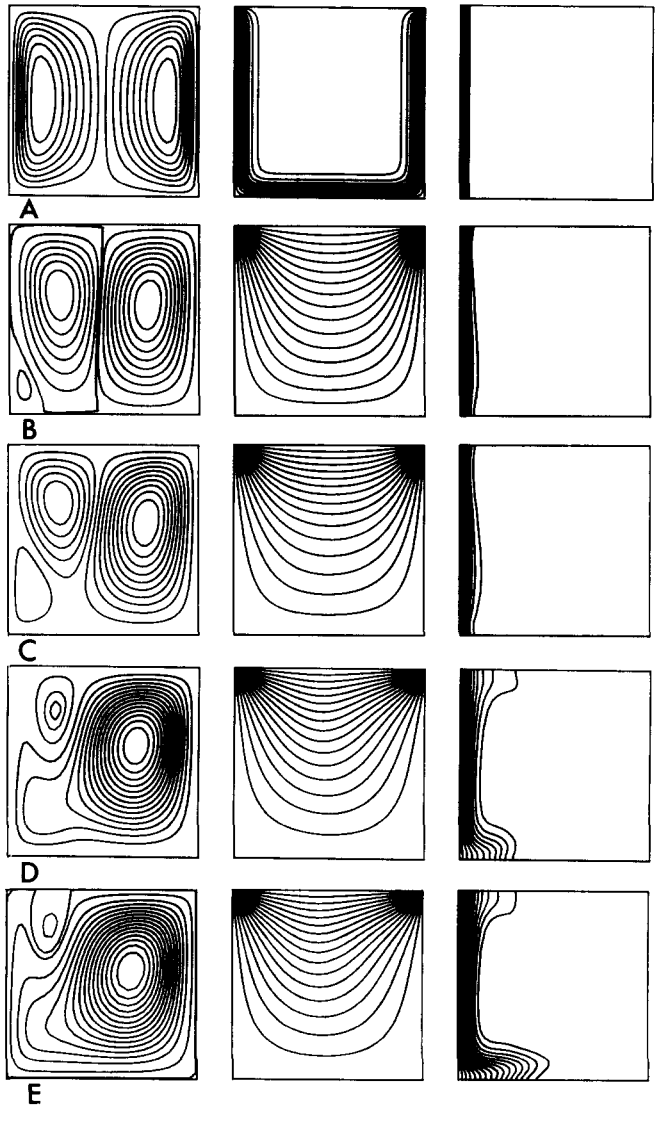


*Figure 13* Time evolution of the velocity, temperature and concentration fields for (a) $\tau = 0.0001$, (b) $\tau = 0.50$, (c) $\tau = 2.50$, (d) $\tau = 3.50$, (e) $\tau = 5.0$ (Notice that the initial phase of convection is dominated by thermal effects [two-cell structures as in Figure 3].)

cells on either side of the middle one start merging together and, consequently, the middle cell becomes weaker (Figure 13d). Later, a large, counterrotating, single cell is formed, with the middle cell confined to a relatively narrow region near the top corner of the left wall. After this time (i.e., for $\tau > 3.5$), the solution becomes periodic with the corner cell periodically increasing and decreasing in size. Hence, the large single cell is formed due to the augmentation of solutal and thermal buoyancies, while the smaller corner cell is induced by thermal buoyancy alone. This interaction is found to give rise to the instability.

To understand the phenomenon further, the phase portraits and power spectra of the solutions have been obtained for different $Ra_T$. Power spectra have been computed from the time series of species concentration using well-known, discrete FFT techniques and a square window (Press et al. 1992). The time history of various quantities has been generated at a point near the bottom left corner (0.08, 0.08).

An interesting feature exhibited by the system is the occurrence of oscillatory solutions at a Rayleigh number as low as 3,000. Figure 14 shows the large-time oscillations in the species concentration at the diagnostic node. The corresponding phase plane behavior and the normalized power spectrum are shown in Figure 15a. The phase portrait shows a limit cycle behavior, and the existence of a single dominant frequency in the power spectrum shows that the solution is of period one. Detailed examination of the solutions indicated that the instability is caused by the secondary flow induced due to interaction between the thermal and solutal boundary layers. Figure 16 shows the stream-function plots at three different instants of time for $Ra_T = 3 \times 10^3$. It can be clearly seen that the corner cell decreases in size. The stream-function plots shown in Figure 16 show a sequence of events over half the period of oscillation. Events during the other half period are essentially similar, except that the cell increases in size. It is interesting to note that these secondary corner vortices are found to be present even when the solution is steady. However, their size is relatively much smaller and does not change with time.

Further period doublings $P_2$ and $P_4$ have been observed at Rayleigh numbers $1.15 \times 10^4$ and $1.35 \times 10^4$, respectively. Phase plane behavior and the power spectrum for the $P_2$ solution is shown in Figure 15b. Stream-function plots for the

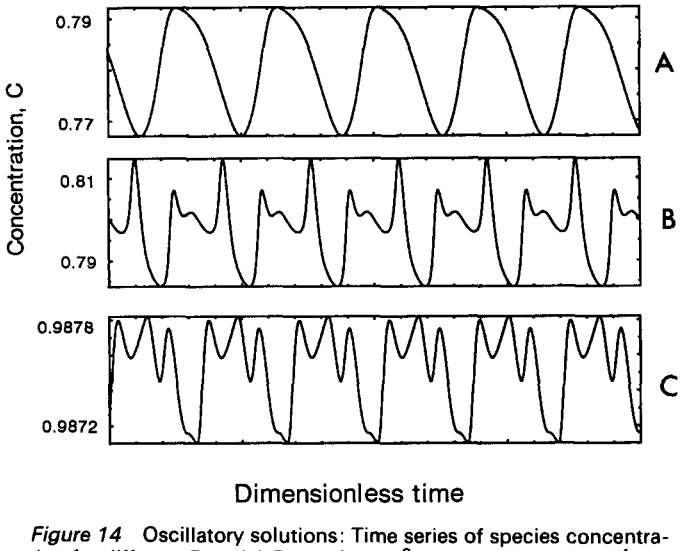


*Figure 14* Oscillatory solutions: Time series of species concentration for different $Ra_T$: (a) $Ra_T = 3 \times 10^3$, (b) $Ra_T = 1.15 \times 10^4$, (c) $Ra_T = 1.4 \times 10^4$

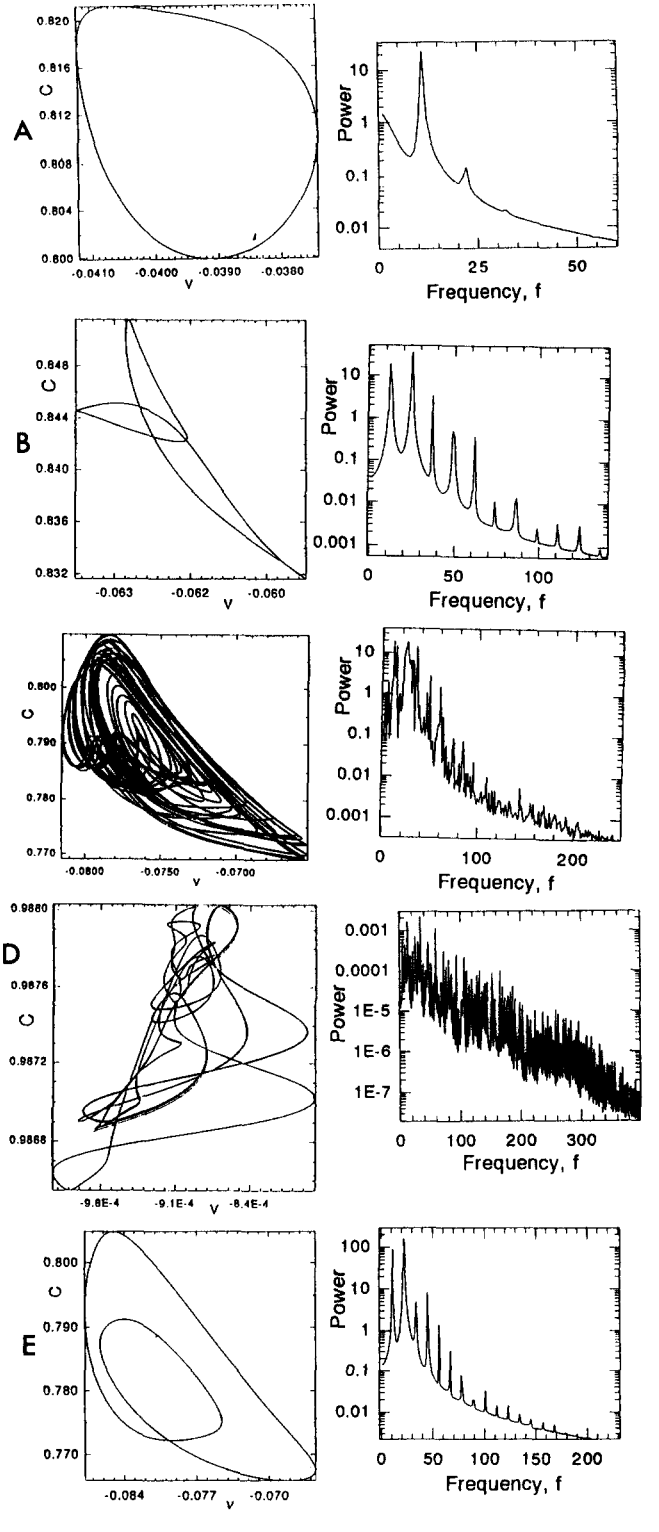


*Figure 15* Phase portraits ($C$ versus $v$) and normalized power spectra ($C$) at the point (0.08, 0.08): (a) $Ra_T = 3 \times 10^3$, (b) $Ra_T = 1.15 \times 10^4$, (c) $Ra_T = 1.4 \times 10^4$, (d) $Ra_T = 1.9 \times 10^4$, (e) $Ra_T = 2.5 \times 10^4$

$P_2$ solution at three different instants of time are shown in Figure 17 for half the period of oscillation. The corresponding $P_4$ solution is qualitatively similar and hence is not shown here. Chaotic solutions ($N$) marked by irregular, tangled paths in the phase plane together with the presence of broad-band noise in

the power spectra have been first observed at a Rayleigh number of $1.45 \times 10^4$. This chaotic regime extended up to $Ra_T = 1.9 \times 10^4$. Phase plane behavior and power spectra for two chaotic solutions are shown in Figures 15c and 15d. A calculation of the Lyapunov exponents based on the algorithm of Wolf et al. (1985) showed that for this range, the maximum Lyapunov exponent is positive. Since the Lyapunov exponent gives an indication of the growth rate of initial perturbations, a positive exponent confirms the presence of chaos in the system. Further increase in the Rayleigh number resulted in reverse transition—a situation in which the solutions reverted back to the periodic type and eventually reached a stable, steady state. Figure 15e shows the phase plane and power spectrum for a solution during reverse transition. Hence, in the Rayleigh number range of $3 \times 10^3$–$3 \times 10^4$, a complete spectrum of period doublings and period halvings has been observed.

As noted earlier, stable, steady-state solutions could not be obtained above a Rayleigh number $Ra_T = 10^6$ when the Lewis number is fixed at 10. An examination of the time series, phase plane behavior of the system and the power spectrum showed that a simple periodic solution has been obtained. Hence, this bifurcation point represents a transition from steady to periodic convection. Limit cycle behavior for this Rayleigh number is shown in Figure 18. For this Lewis number (10), the route to chaos has been found to be essentially similar, except that the bifurcation points are different.

In conclusion, the system has been found to exhibit the route $S \rightarrow P \rightarrow P_2 \rightarrow P_4 \rightarrow N$. Subharmonic bifurcations above $P_4$ have not been observed. It is difficult to capture these bifurcations, as the interval between successive bifurcations decreases rapidly with increasing $Ra_T$. However, a bifurcation diagram obtained by plotting the successive maxima in concentration against the Rayleigh number did not show any subharmonic bifurcations above $P_4$. In view of the fact that confined buoyant flows exhibit only a few degrees of freedom, we believe that for this system only four bifurcations are needed before chaos is reached.

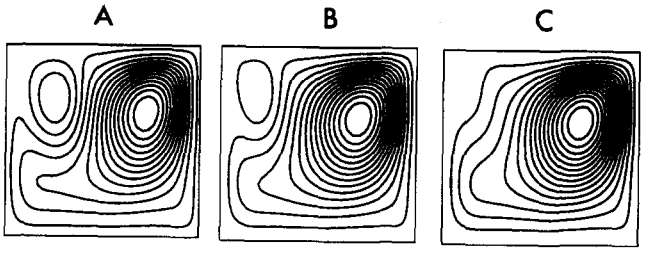


*Figure 16* Simple periodic solution at $Ra_T = 3 \times 10^3$: Stream-function plots at three different instants of time shown for half the period of oscillation

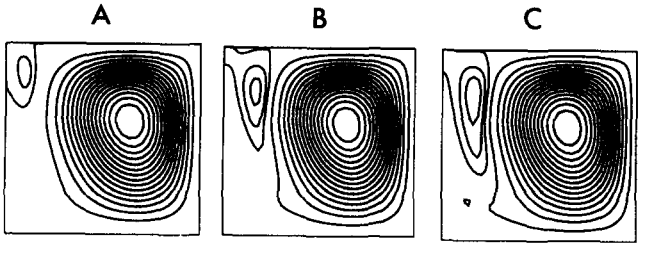


*Figure 17* $P_2$—Periodic solution at $Ra_T = 1.15 \times 10^4$: Stream-function plots at different instants of time shown for half the period of oscillation

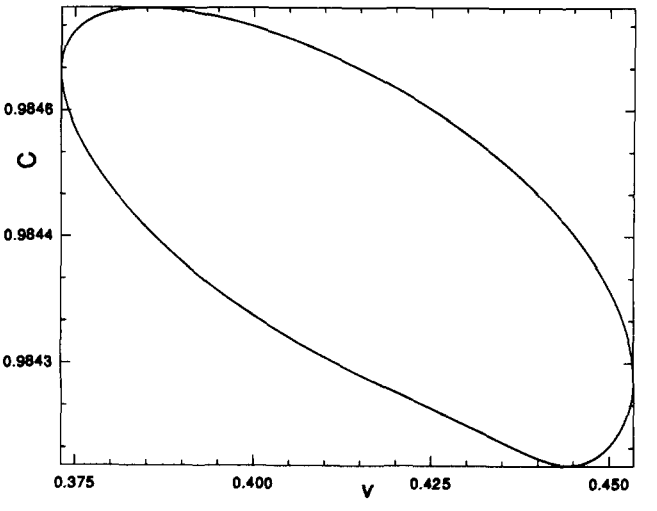


*Figure 18* Limit cycle behavior at $Ra_T = 10^6$ for Le = 10

## 4. Conclusions

The problem of thermosolutal convection in a rectangular enclosure has been studied for a case in which the bottom and sidewalls are heated. Complex, multicell structures and unsteady solutions have been obtained depending on the parameters. Steady-state solutions could not be obtained in the Rayleigh number range of 3,000–30,000 for a Lewis number of 100. Results obtained using an unsteady model indicated that successive flow bifurcations take place in this range until the flow becomes chaotic. Additional increase in the Rayleigh number brought about a reverse transition to steady state.

## Acknowledgments

Computations reported in this paper have been carried out on the COSMOS-486 super-mini at C-MMACS using an i860 vector coprocessor. The author gratefully acknowledges the support and encouragement provided by Dr. K. S. Yajnik, Head, C-MMACS.

## References

Béghein, C., Haghighat, F. and Allard F. 1992. Numerical study of double-diffusive natural convection in a square cavity. *Int. J. Heat Mass Transfer*, **35**, 833–846

Bergman, T. L. and Ungan, A. 1988. A note on lateral heating in a double-diffusive system. *J. Fluid Mech.*, **194**, 175–186

Bontoux, P., Gilly, B. and Roux, B. 1979. Natural convection in cavities for high Rayleigh numbers. In *Notes on Numerical Fluid Mechanics*, Vol. 2, E. H. Hirschel (Ed.), Vieweg, Braunschweig, 22–35

Chang, J. and Lin, T. F. 1993. Unsteady thermosolutal opposing convection of liquid-water mixture in a square cavity—II. Flow structure and fluctuation analysis. *Int. J. Heat Mass Transfer*, **36**, 1333–1345

Chang, J., Lin, T. F. and Chien, C. H. 1993. Unsteady thermosolutal opposing convection of a liquid-water mixture in a square cavity—I. Flow formation and heat and mass transfer characteristics. *Int. J. Heat Mass Transfer*, **36**, 1315–1331

de Vahl Davis, G. 1983. Natural convection of air in a square cavity: a benchmark numerical solution. *Int. J. Num. Meth. Fluids*, **3**, 249–264

Feigenbaum, M. J. 1979. The onset spectrum of turbulence. *Phys. Letters*, **A74**, 375–378

Furlong, K. P., Hanson, R. B. and Bowers, J. R. 1991. Modeling thermal regimes. In *Contact Metamorphism*, D. M. Kerrick (Ed.). *Rev. Mineral.*, **26**, 437–505

Gill, P. E. and Miller, G. F. 1972. An algorithm for the integration of unequally spaced data. *Comp. Journal*, **15**, 80–83

Gollub, J. P. and Bensen, S. V. 1980. Many routes to turbulent convection. *J. Fluid Mech.*, **100**, 449–470

Hageman, L. A. and Young, D. M. 1981. *Applied Iterative Methods.* Academic Press, New York

Han, H. and Kuehn, T. H. 1991. Double-diffusive natural convection in a vertical rectangular enclosure—I and II. *Int. J. Heat Mass Transfer*, **34**, 449–471

Hirsch, R. S. 1975. Higher order accurate difference solutions of fluid mechanics problems by a compact differencing technique. *J. Comp. Phys.*, **19**, 90–109

Hirsch, R. S. 1983. Higher order approximations in fluid mechanics—compact to spectral. In *Computational Fluid Dynamics—VKI Lecture Series, 1983-84.* Von Karman Institute for Fluid Dynamics, St. Rhode Genes, Belgium, 1–116

Jiang, H. D., Ostrach, S. and Kamotani, Y. 1988. Thermosolutal convection with opposed buoyancy forces in shallow enclosures. *ASME-HTD*, **99**, 53–66

Kamotani, Y., Wang, L. W., Ostrach, S. and Jiang, H. D. 1985. Experimental study of natural convection in shallow enclosures with horizontal temperature and concentration gradients. *Int. J. Heat Mass Transfer*, **28**, 165–173

Kessler, R. 1987. Nonlinear transition in three-dimensional convection. *J. Fluid Mech.*, **174**, 357–379

Landau, L. D. and Lifshitz, E. M. 1982. *Fluid Mechanics, Course of Theoretical Physics.* Vol. 6, Pergamon Press, New York

Libchaber, A. and Maurer, I. 1982. A Rayleigh-Bénard experiment: Helium in a small box. In *Nonlinear Phenomena in Phase Transitions and Instabilities*, T. Riste (Ed.). 259–286

Lorenz, E. N. 1989. Computational chaos—A prelude to computational instability. *Physica D*, **37**, 126–145

Moore, D. R., Toomre, J., Knobloch, E. and Weiss, N. O. 1983. Period doubling and chaos in partial differential equations for thermosolutal convection. *Nature*, **303** (23 June), 348–352

Ostrach, S. 1983. Fluid mechanics in crystal growth—The 1982 Freeman scholar lecture. *ASME J. Fluids Engg.*, **105**, 5–20

Patankar, S. V. 1980. *Numerical Heat Transfer and Fluid Flow.* Hemisphere, Washington, D.C.

Press, W. H., Flannery, B. P., Teukolsky, S. A. and Vetterling, W. T. 1992. *Numerical Recipes in FORTRAN—The Art of Scientific Computing.* 2nd ed., Cambridge University Press, Cambridge, UK

Reay, D. A. 1979. *Heat Recovery Systems—A Directory of Equipment and Techniques.* E. & F. N. Spon, London

Roberts, G. O. 1971. Computational meshes for boundary layer problems. *Proc. 2nd Int. Conf. on Numerical Methods in Fluid Dynamics*, M. Holt (Ed.), Springer-Verlag, Berlin, 171–177

Ruelle, D., Takens, F. and Newhouse, S. E. 1978. Occurrence of strange axiom A attractors near quasi-periodic flows in $T^m$, $m \geq 3$. *Comm. Math. Phys.*, **64**, 35–40

Settari, A. and Aziz, K. 1973. A generalization of the additive-correction methods for the iterative solution of matrix equations. *SIAM J. Numer. Analysis*, **10**, 506–521

Trevisan, O. V. and Bejan, A. 1987. Combined heat and mass transfer by natural convection in a vertical enclosure. *ASME J. Heat Transfer*, **109**, 104–112

Turner, J. S. 1975. Laboratory experiments on double-diffusive instabilities. *Adv. Chem. Phys.*, **32**, 135

von Rosenberg, D. U. 1969. *Methods for the Numerical Solution of Partial Differential Equations.* American Elsevier, New York

Wachspress, E. L. 1979. *Iterative Solution of Elliptic Systems and Applications to the Neutron Diffusion Equations of Reactor Physics.* Prentice-Hall, Englewood Cliffs, N.J.

Weaver, J. A. and Viskanta, R. 1991a. Natural convection due to horizontal temperature and concentration gradients—1. Variable thermophysical property effects. *Int. J. Heat Mass Transfer*, **34**, 3107–3120

Weaver, J. A. and Viskanta, R. 1991b. Natural convection due to horizontal temperature and concentration gradients—2. Species interdiffusion, Soret and Dufour effects. *Int. J. Heat Mass Transfer*, **34**, 3121–3133

Wolf, A., Swift, J. B., Swinney, H. L. and Vastano, J. A. 1985. Determining Lyapunov exponents from a time series. *Physica*, **16D**, 285–317

Yang, K. T. 1988. Transitions and bifurcations in laminar buoyant flows in confined enclosures. *ASME J. Heat Transfer*, **110**, 1191–1204